Faraday Discussions

The Influence of Iodide on the Solution-Phase Growth of Cu Microplates: A Multi-Scale Theoretical Analysis from First Principles

Journal:	*Faraday Discussions*
Manuscript ID	FD-ART-11-2021-000091
Article Type:	Paper
Date Submitted by the Author:	21-Nov-2021
Complete List of Authors:	Kim, Junseok; Pennsylvania State University, Chemical Engineering Fichthorn, Kristen; Pennsylvania State University,

The Influence of Iodide on the Solution-Phase Growth of Cu Microplates: A Multi-Scale Theoretical Analysis from First Principles

*Junseok Kim[1] and Kristen A. Fichthorn[1,2]**

Department of Chemical Engineering[1] and Department of Physics[2]; The Pennsylvania State University; University Park, PA 16802 USA

*Email: fichthorn@psu.edu

Abstract

We use first-principles density functional theory (DFT) to quantify the role of iodide in the solution-phase growth of Cu microplates. Our calculations show that a Cu adatom binds more strongly to hcp hollow sites than fcc hollow sites on iodine-covered Cu(111) – the basal facet of two-dimensional (2D) Cu plates. This feature promotes the formation of stacking faults during seed and plate which, in turn, promotes 2D growth. We also found that iodine adsorption leads to strong Cu atom binding and prohibitively slow diffusion of Cu atoms on Cu(100) – a feature that promotes Cu atom accumulation on the {100} site facets of a growing 2D plate. Incorporating these insights into analog experiments, in which we initiated the growth of Cu plates from small seeds consisting of magnetic spheres, we confirmed that two or more stacking faults are required for lateral plate growth, consistent with prior studies. Moreover, plates can take on a variety of shapes during growth: from triangular and truncated triangular to round and hexagonal – consistent with experiment. Using absorbing Markov chain calculations, we assessed the propensity for 2D vs. 3D kinetic growth of the plates. At experimental temperatures, we predict plates can grow to achieve lateral dimensions in the 1-5micron range, as observed in experiments.

Introduction

Understanding the growth of two-dimensional (2D) fcc metallic nanomaterials is both fundamentally and technologically important. From a technological perspective, the unique structure and properties (mechanical, plasmonic, electrical, and catalytic) of 2D metal nanoplates and microplates makes them promising for a range of applications,[1–5] including catalysis and electrocatalysis,[6–11] sensing,[12–15] conductive inks,[16] theranostics,[17–20] and multi-functional property enhancement of polymer nanocomposites.[21] Many of the beneficial properties of 2D nanoplates, microplates, and nanoprisms stem from their surface plasmon resonance (SPR) and surface enhanced Raman scattering (SERS) properties, which depend on the plate dimensions. [22–24] Thus, it is of interest to obtain precise control of plate dimensions and shapes when they are synthesized.

One way to synthesize 2D metallic nanostructures is through solution-phase methods.[25–30] In these syntheses, a metal salt is reduced by solvent and/or solution-phase additives. Metal atoms and ions aggregate to form nuclei, which evolve to seeds. It has been suggested that 2D nanocrystals originate from plate-like seeds.[29,31] Capping agents, or additives present in the synthesis, can facilitate the formation of 2D structures from seeds.

As shown in **Figure 1**, fcc metal nanoplates and their putative seeds possess relatively large, basal {111} facets on the top and bottom, while the sides contain a mix of {111}, {100}, and possibly higher-index facets. Many studies have emphasized the need for plates to have stacking faults and/or twin boundaries to maintain their 2D geometry.[32–36] Recently, Tan et al.[35] showed that the number of the twins affects the symmetry of the seed, which determines the final structure of the plate – or whether a plate will form at all.

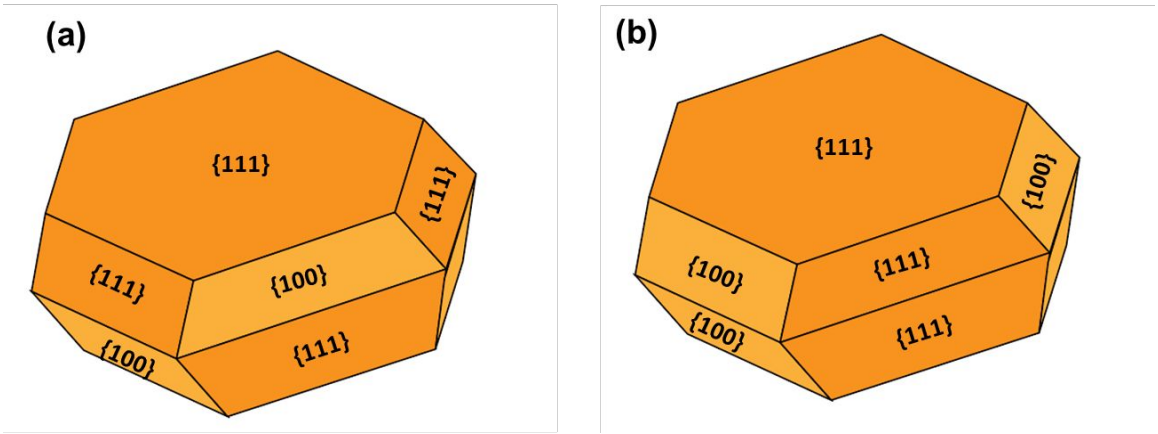

Figure 1. Schematic of two popular models for fcc metal nanoplate geometries. (a) The alternating facet model; and (b) The mirror symmetry model.

In this study, we use multi-scale theoretical methods to examine the role of iodide (I^-) in producing Cu microplates in an experimental solution-phase synthesis.[37] In a previous study, we used first-principles, density-functional theory (DFT) to show that iodide stabilizes Cu(111) facets (lowers their surface energy) to a greater degree than it stabilizes Cu(100) facets, providing a thermodynamic driving force for plate growth from a seed.[37] While this thermodynamic driving force can be helpful in creating large basal {111} facets, it does not explain plate shapes or why, for example, plate seeds do not transform to other {111}-faceted shapes, such as octahedra, to maximize the bulk energy and minimize the surface energy. To address these questions, we use DFT calculations to quantify energies and kinetics relevant for the growth of plate-like Cu seeds to 2D crystals. We construct plate-like seeds containing different numbers of stacking faults from magnetic spheres and guided by DFT energies, we grow the plates by adding spheres to the most energetically preferred sites on the sides of the plates. Incorporating the DFT rates into absorbing Markov chain calculations, we quantify net rates for inter-facet transport, which allows us to predict the size of the basal {111} facets. Our

studies agree with experiment and confirm the important role of iodide in facilitating plate growth.

Results and discussion

Cu Atom Binding on I-Covered Cu Surfaces

In previous work, we used DFT to study likely surface environments for Cu microplates to form and grow from $CuCl_2$ salt in aqueous solution containing hexadecylamine (HDA) and NaI.[37] These studies showed that solution-phase I^- displaces Cl^- (from the $CuCl_2$ salt) and HDA from both Cu(111) and Cu(100) under the synthetic conditions that were the most conducive to plate formation and growth.[37] The predicted structures of Cu(100) and Cu(111) under these conditions are shown in **Figure 2.**

For Cu(111), iodine has the $(\sqrt{3}x\sqrt{3})R30°$ lattice structure at 1/3 monolayer (ML) coverage,[37] where a ML is defined as the ratio of adsorbed I atoms to the number of Cu atoms in the topmost surface layer. Iodine atoms can be placed on either fcc or hcp hollow sites of Cu(111), as shown in **Figure 2(a)** and **2(b)**, respectively. Interestingly, both structures show similar binding energies for iodine [-1.90/1.91 eV for **Figure 2(a)/(b)**]. For Cu(100), a c(2x2) lattice structure with 1/2 ML coverage was found to be the most favorable structure, [37] as shown in **Figure 2(c)**.

Figure 2 also shows possible binding positions for a Cu adatom on the iodinated Cu surfaces, with corresponding binding energies listed in **Table 1**. As we see in **Figures 2(a) and 2(b)**, a Cu adatom has two possible binding sites on the Cu(111) surfaces. Cu adatoms exhibit the strongest binding in three-fold fcc or hcp hollow sites ① and they coordinate with three neighboring

iodine atoms. The binding in site ② is relatively weaker and the Cu adatom establishes two-fold coordination with its neighboring I atoms. Interestingly, a Cu adatom binds more strongly to the hcp hollow site of Cu(111) in the presence of iodine [**Figure 2(b)**], unlike bare Cu(111). This binding preference promotes the formation of stacking faults which have been linked to microplate growth. [32–36]

Though we tried several possible initial sites on Cu(100), we found only one favorable binding site for a Cu adatom ①, in which the atom resides below an adsorbed I on a fourfold hollow site. As we see in **Table 1**, the Cu binding energy is strong in this site compared to the sites on Cu(111).

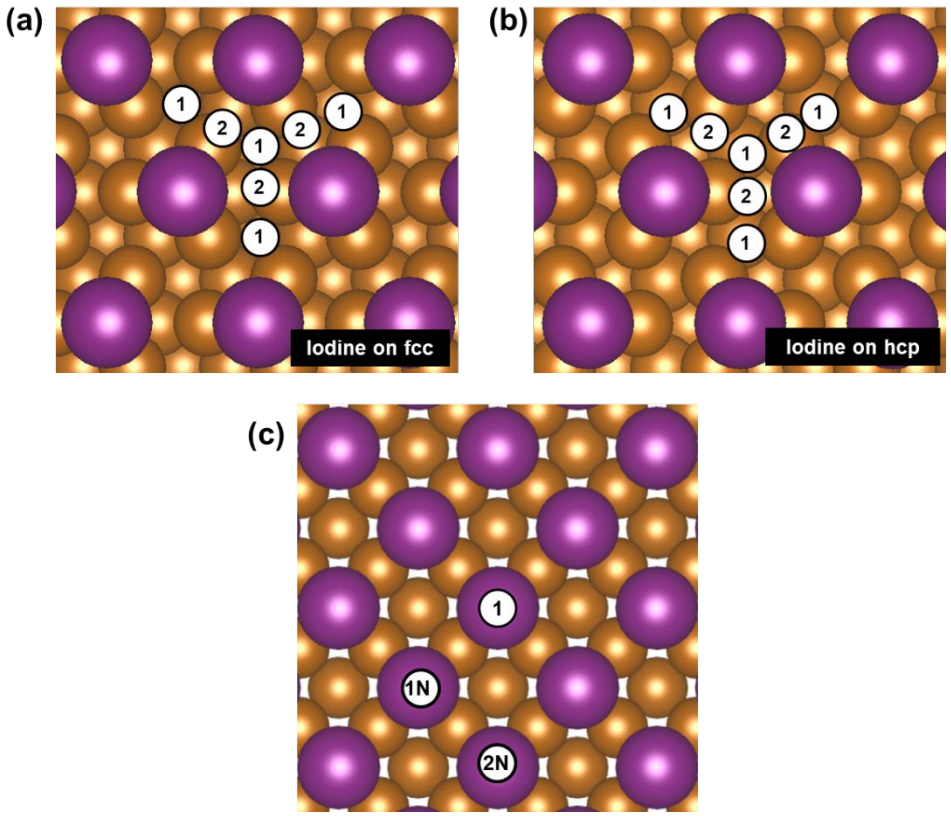

Figure 2. Binding sites for Cu adatom on Cu surfaces with adsorbed I for: (a) 1/3 ML-I on fcc hollow sites of Cu(111); (b) 1/3 ML-I on hcp hollow sites of Cu(111); and (c) 1/2 ML-I on hollow sites of Cu(100). A Cu atom has two different binding sites on the {111} facets – fcc and hcp three-fold hollow sites – and one binding site on {100} – in a four-fold hollow site beneath an adsorbed I atom. First- (1N) and second neighbor (2N) sites are indicated on the {100} surface. Cu is shown in orange, and I is purple.

Table 1. Binding energies and surface diffusion energy barriers for a Cu adatom on iodinated Cu surfaces.

Surface	Binding Position	Binding Energy (eV)	Forward (Reverse) Diffusion Barrier (eV)
Figure 1(a)	fcc ①	-3.51	① → ②: 0.12 (<0.01)
	hcp ②	-3.39	
Figure 1(b)	hcp ①	-3.53	① → ②: 0.13 (<0.01)
	fcc ②	-3.39	
Figure 1(c)	subsurface-hollow ①	-5.03	①→① (1N) Exchange: 2.01 ①→① (2N) Hop: 1.33

We investigated the surface diffusion of a Cu adatom on each of the surfaces in **Figure 2** using the climbing-image nudged elastic band (CI-NEB) method.[38] The diffusion energy barriers between neighboring binding sites are listed in **Table 1**. Here, we see that diffusion on 1/3 ML I-Cu(111) proceeds relatively rapidly. On 1/2 ML I-Cu(100), we investigated diffusion to two

neighboring binding sites – the first (1N) and second (2N) neighbor subsurface hollow sites. We found diffusion to the first-neighbor binding site occurs via an exchange process, in which the Cu adatom takes the place of a Cu surface atom, which then becomes the adatom. We find hopping is preferred for diffusion to the second-neighbor site. As we see in **Table 1**, both diffusion pathways require prohibitively high energy barriers so that the diffusion of a Cu adatom is virtually impossible on 1/2 ML I-Cu(100) under experimental conditions. Thus, the adsorption of iodine leads to a stronger binding and slower diffusion of a Cu adatom on Cu(100) than Cu(111), which indicates a preferred accumulation of Cu on Cu(100). As we will elaborate below, this binding preference contributes to the lateral growth of Cu plates by promoting the accumulation of Cu on the side {100} facets of the plates.

Preferred Microplate Shapes

As shown in **Figure 1**, two types of plate structures have been identified in previous studies: the alternating facet model [**Figure 1(a)**] and the mirror-symmetry facet model [**Figure 1(b)**]. As has been discussed previously,[35,37] a plate with alternating facets occurs when the number of stacking faults is even, while a plate with mirror symmetry is formed with an odd number of stacking faults. Here, we investigate these plate-shape models in the context of plate growth with the DFT binding energies in **Table 1**.

We first consider a seed plate with no stacking faults – the single crystal shown in **Figure S1** in the Electronic Supporting Information (ESI). When a plate seed has no stacking faults, it has alternating side facets, as shown in **Figure 1(a)**, and an octahedron was obtained with addition to {100} sites only (**Figure S1**). When a plate has one stacking fault, it has the mirror-symmetry facet model shown in **Figure 1(b)** and preferential Cu atom accumulation on {100} resulted in a

triangular plate with all {111} surfaces (**Figure S2**). With further growth of the {111} facets, the final shape would be a 3D trigonal bipyramid and **not** a 2D plate.

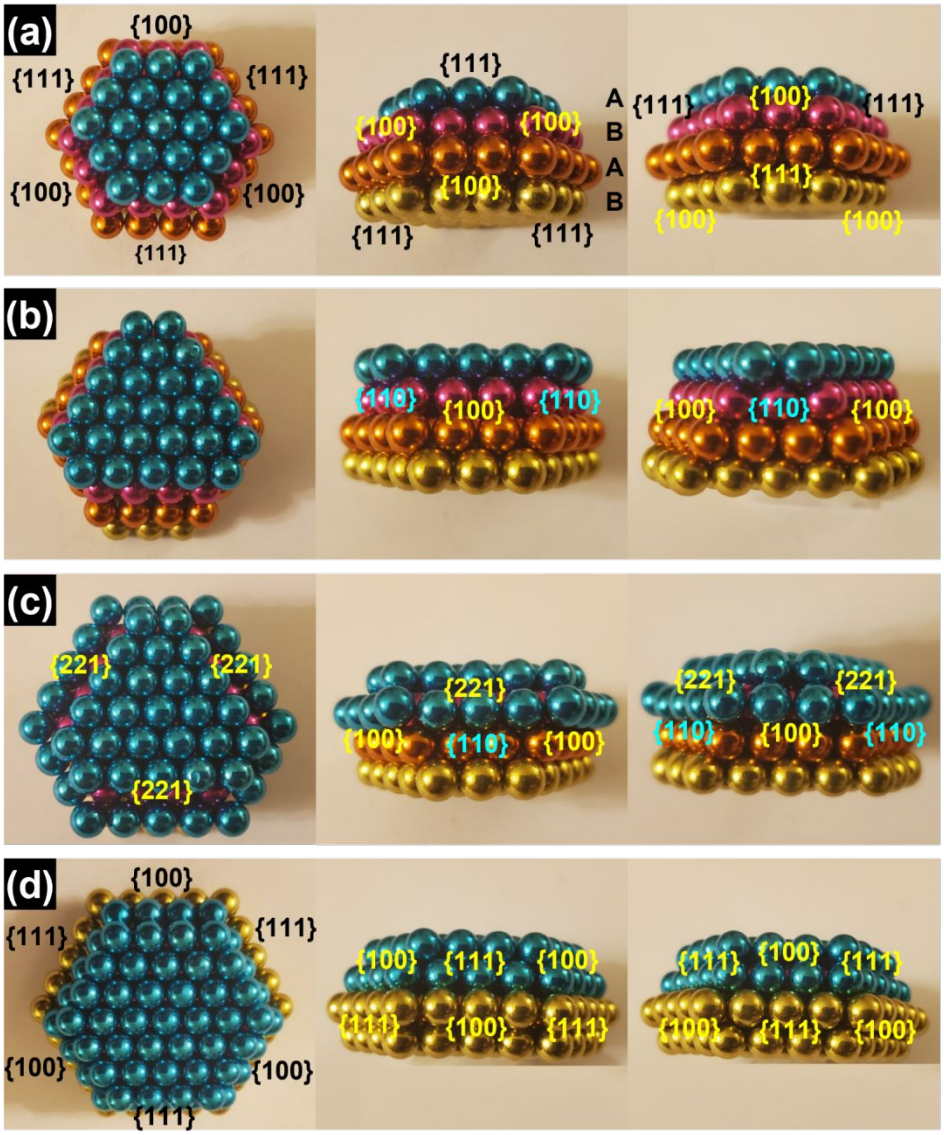

Figure 3. Growth of an hcp plate seed, as a model of a larger plate containing two stacking faults. A top-down view of a basal facet is shown in the left panel and two different side views are shown in the center and right panels. In (a) we show three views of the initial seed, which the alternating facet structure in **Figure 1(a).** The center panel indicates the hcp layer stacking.

In (b) we show the structure after adding an atom to each of the four-fold {100} sites. After filling in all the {100} and {110} sites, we generate three rows of {221} sites and {100} sites in the middle, as shown in (c). Subsequent to filling in the {221} and {100} sites, we achieve the hexagonal structure in (d), which regenerates the structure in (a).

We find lateral growth of the plate seeds is possible when there are two or more stacking faults. First, we grow an hcp plate as a model for a plate containing two stacking faults in the center. The growth progression is shown in **Figure 3**. After adding an atom to each {100} site of the initial seed in **Figure 3(a)**, we achieve the structure in **Figure 3(b)**. We see in the side views to **Figure 3(b)** that this creates {110} sites. We regard {110} (and sites on facets with higher indices) to be the most energetically preferred binding sites because of the relatively higher surface energies of such facets. After filling in all the {110} and {100} binding sites in **Figure 3(b)**, we attain the structure in **Figure 3(c)**, where we generated three rows of {221} and {100} sites in the middle. After filling in all the {221} and {100} sites, we achieve the hexagonal structure in **Figure 3(d)**, which creates a larger version of the structure in **Figure 3(a)**. This process can be repeated to achieve continuous lateral growth of the plate. We observed a similar growth progression when we varied the positions of the two stacking faults, as can be seen in **Figure S3**, and when we used a plate containing three stacking faults, as we see in **Figure S4**. In all cases with two or more tacking faults, we could create a larger version of our initial seed by adding Cu atoms to the sites with the highest binding energies.

Truncated triangular and hexagonal plate shapes have been observed in many experiments.[25,34–37,39] In an attempt to understand if or how these shapes depend on the number of stacking faults or the filling sequence of the side facets, we grew plates beginning with

various seed configurations. The observation that perhaps best summarizes our attempts in this regard is shown in **Figure 4**.

In **Figure 4**, we show a sequence of snapshots as we grew a plate from a triangular seed containing two stacking faults. We see that the plate evolves through a progression of shapes as we fill in the energetically preferred binding sites on the sides of the plates – from a triangle in **Figure 4(b)** to a round shape in **Figure 4(c)** to a truncated triangle in **Figure 4(f)** to a near hexagon in **Figure 4(h)**. Thus, we see that shape evolution to equilateral and truncated triangles, hexagons, and round shapes are all possible during lateral growth if there are two or more stacking faults, which is also observed in experiment.[35] Nevertheless, we found that most of the plate shapes during the lateral growth are hexagonal and truncated triangular structures, consistent with experiment.[37]

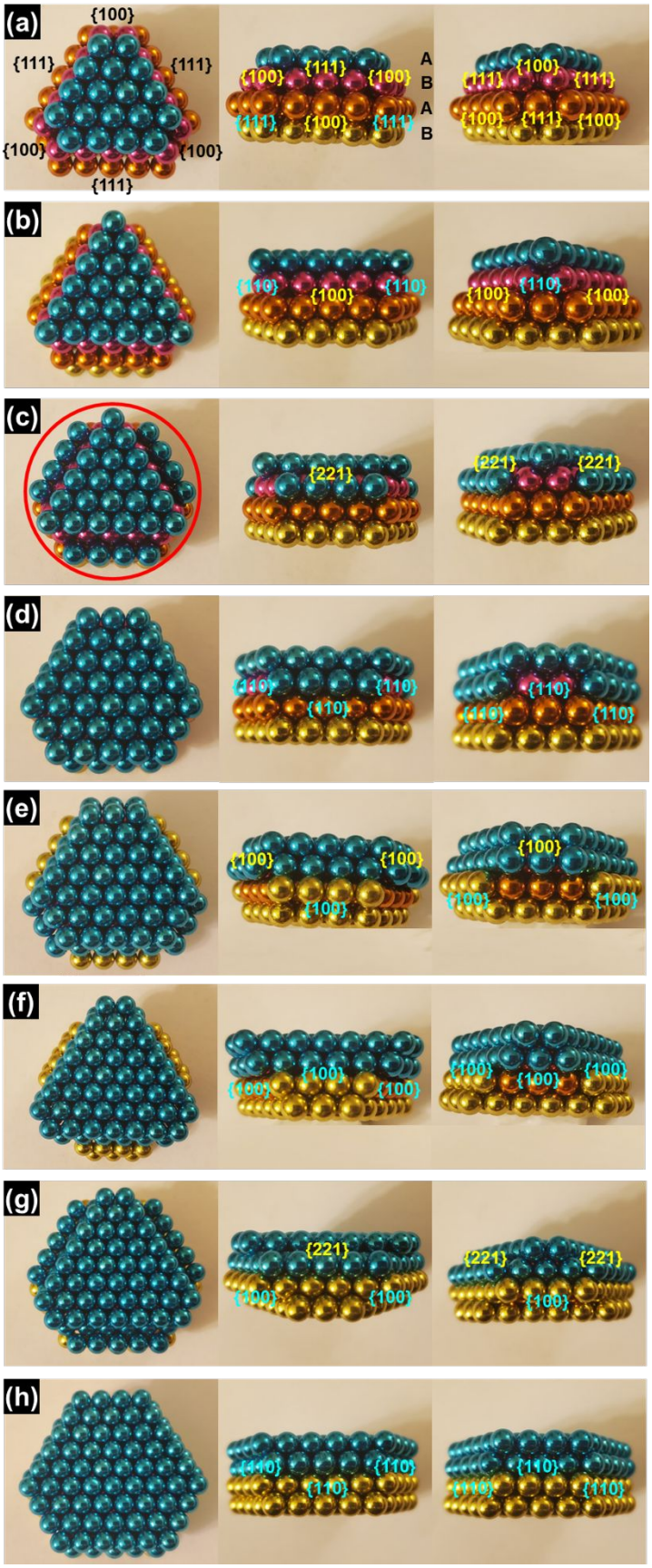
(a)
{100}
{111}
{111}
{100}
{100}
{111}
A
B
A
B
(b)
{110}
{100}
{110}
(c)
{221}
(d)
{110}
(e)
{100}
(f)
(g)
{221}
(h)

Figure 4. Sequence of shapes that evolve as we grow a plate by adding spheres to sites with the highest binding energies on the sides of the plate. A top-down view of a basal facet is shown in the left panel and two different side views are shown in the center and right panels. The initial shape in (a) is a truncated triangular seed containing two stacking faults. A triangle is formed in (b), which transforms to a round shape in (c). After transforming between various truncated triangular and hexagonal shapes in (d)-(g) a near hexagon emerges in (h).

Cu Atom Inter-Facet Transport on I-Covered Cu Surfaces

It is clear from **Table 1** that there is a strong thermodynamic driving force for Cu atoms to stick to the {100} sides of a growing Cu plate. By following an evolution sequence in which Cu atoms always bind to the sites with the highest binding energies, we showed that lateral plate growth could be maintained. However, plate growth is a kinetic process. If the Cu atom deposition rate (or reduction rate) is large compared to diffusion rates, atoms deposited on the large, basal facets of the plates will not reach the sides of the plates on the time scale of deposition. In this case, Cu atoms will accumulate on the basal facets and grow the plates vertically instead of laterally.

To assess the propensity of the plates to exhibit lateral growth, we examined the elementary steps underlying inter-facet transport on an iodine-covered Cu plate. We investigated two facet boundaries suggested by the two typical models for the sides of fcc plates, shown in **Figure 1**.[33,35,36,39–41] Both models contain {111}-{100} and {111}-{111} facet boundaries, and we employed two different Cu slabs to characterize inter-facet diffusion. These two slabs are shown in **Figure S5**.

We first consider diffusion between the {100} and {111} facets. Iodine can be adsorbed to either fcc or hcp hollow sites on Cu(111) and we consider both of these scenarios. **Figure 5** shows Cu binding sites and diffusion pathways for the case that iodine is adsorbed on fcc hollow sites on Cu(111). As shown in **Figure 5(a)**, we identified four different hollow sites on {100} and six fcc and hcp hollow sites on {111} near the {100}-{111} edge. The corresponding binding energies are listed in **Table S1**.

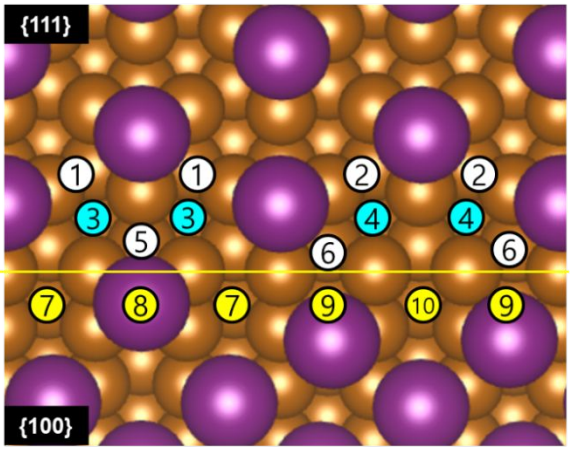

(a)

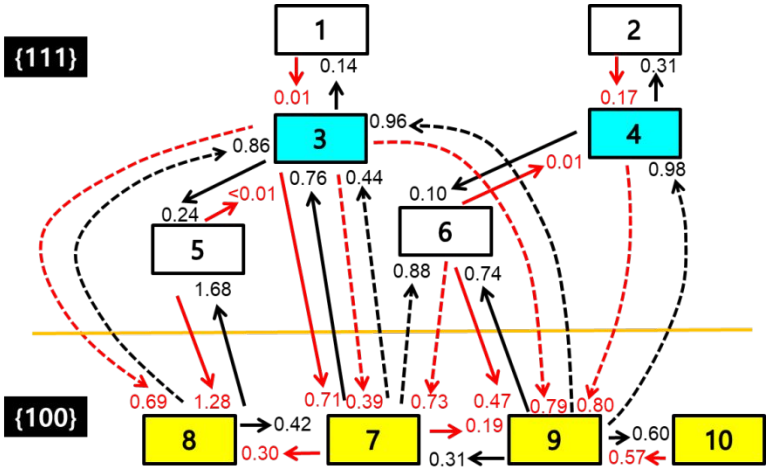

(b)

Figure 5. (a) Binding sites for Cu adatom near the {111}-{100} edge when iodine is placed on fcc hollow sites on {111} – viewed from the perpendicular direction to {111} (Cu atoms are orange and I atoms are purple); and (b) the inter-facet diffusion pathways. Numbers at the end of each arrow denote the diffusion energy barrier (in eV) for that pathway. The red arrows denote lower barrier pathways in the forward-reverse pair. Arrows with solid lines represent hopping, while arrows with dashed lines represent exchange diffusion. Hcp{111} binding sites are shown in white, fcc{111} binding sites are shown in turquoise, and four-fold hollow sites on {100} are shown in yellow.

In **Table S1**, we see the binding energies on sites ① and ② on the inter-facet slab are similar to those on sites on the flat 1/3 ML I-Cu(111) surface (compare **Tables 1** and **S1**). This result implies the inter-facet slab captures binding on a flat Cu surface away from the edge. On the other hand, Cu adatom binding on sites near the {100} edge is much weaker than on flat Cu(100), even though it is stronger than binding on {111} (see **Table S1**). In addition, subsurface binding is not preferred near the {100}-{111} edge.

In **Figure 5(b)**, we show our calculated diffusion pathways and energy barriers among the various sites in **Figure 5(a)**. Here, we see that most of the diffusion pathways from {111} to {100} have lower energy barriers than those for the reverse direction, such that {111}→{100} transport is preferred to {100}→{111} transport. This aspect, combined with the strong binding we observe on the flat Cu(100) surface (cf., **Table 1**), leads to our expectation that it would be difficult for Cu atoms to escape from {100} once they reach that facet.

We also investigated a {100}-{111} inter-facet slab in which iodine is adsorbed on hcp hollow sites on {111} (see **Figure S6 and Table S2**). Although there are differences between this system and the system in **Figure 5**, we still find that most of the inter-facet diffusion pathways from {111} to {100} possess lower energy barriers than the reverse direction, as seen in **Figure S6(b)**. Therefore, we can say that whether iodine is placed on fcc or hcp hollow sites on {111}, transport of Cu atoms from {111} to {100} is preferred over the opposite direction.

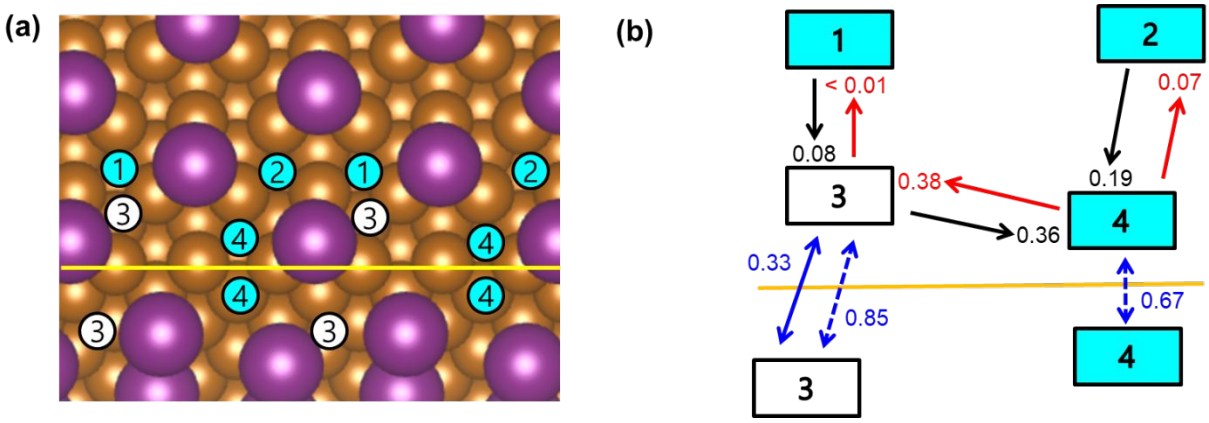

Figure 6. (a) Binding sites for a Cu adatom on the {111}-{111} facet edge when iodine is placed on fcc hollow sites (Cu atoms are orange and I atoms are purple) and (b) inter-facet diffusion pathways. Numbers at the end of each arrow denote the diffusion energy barrier (in eV) for that pathway. The red arrows denote lower barrier pathways in the forward-reverse pair. Arrows with solid lines represent hopping, while arrows with dashed lines represent exchange diffusion. Hcp{111} binding sites are shown in white and fcc{111} binding sites are shown in turquoise.

There are three different configurations for I at the {111}-{111} edge: 1) I adsorbed on fcc hollow sites on both facets; 2) I adsorbed on fcc hollow sites on one facet and hcp hollow sites on the other facet; and 3) I adsorbed on hcp hollow sites on both facets. **Figure 6(a)** shows the

first case, with possible Cu binding sites. In this case, we confirmed that a Cu adatom has similar binding energies for the same binding site on both {111} facets, as listed in **Table S3**. In addition, we found that a fcc site far from the edge has a comparable binding energy (-3.48 eV) to that on flat 1/3 ML I-Cu(111), which shows the reliability of this inter-facet slab. Less states are involved in {111}-{111} diffusion than in {111}-{100} diffusion. We also noted that different symmetries of I are possible when it is placed on fcc sites of both facets. **Figure S7** and **Table S4** summarize this case. **Figures S8** and **S9** summarize the cases for which we have I on fcc sites on one facet and hcp on the other and when we have I in hcp sites on both facets. These calculations showed there is no significant difference in the binding energies and inter-facet diffusion energy barriers compared to those in **Figure 6.** Thus, we expect that whether iodine is absorbed on fcc or hcp hollow sites on {111} we would see similar inter-facet diffusion.

Lateral vs. Vertical Growth of Cu Microplates

Using our calculated diffusion-energy barriers, we assessed the propensity for lateral vs. vertical growth of the Cu microplates. We expect that if the plate dimensions are sufficiently small, atoms can rapidly access the plate sides and accumulate on the energetically favored {100} (or higher index) sites to grow the plates laterally. However, as the plates grow, the mean-first passage time (MFPT) for a deposited atom to reach the sides of a plate will increase, the inter-facet transit rate will decrease, and we will eventually reach a critical plate size at which accumulation begins to occur on the basal facets. Below, we estimate that critical plate size.

To estimate the MFPT for an deposited atom on a basal plate facet to reach the sides of the plate, we use the theory of the absorbing Markov chains.[42,43] We used (and explained) this

method in prior work.[44–46] Briefly, we solve for the average time, considering all possible deposition sites, for a Cu atom deposited on a basal {111} facet to diffuse to a side facet. This involves constructing a Markov matrix to characterize the network of diffusion rates for site-to-site hops/exchanges. There are two kinds of states in the kinetic network: transient states, which can be accessed and vacated an indefinite number of times as the Cu atoms diffuses around on the basal facet, and absorbing states at the sides of the plate. Absorbing states are occupied permanently once they are accessed. Two relevant sub-matrices of the Markov matrix are the transient matrix **T** and the recurrent matrix **R**.[42–44] The MFPT t_M is obtained from the transient matrix as

$$t_M = \overline{p}_0^T \cdot (\mathbf{T} - \mathbf{I})^{-1} \cdot \overline{\tau} \quad , \tag{1}$$

where $\overline{p}_0^T$ is the transpose of the probability vector for each transient state to be initially occupied. For *N* sites (transient states) on the basal facet, each element of $\overline{p}_0$ is 1/*N*, assuming each site is equally likely to be occupied initially. **I** is the identity matrix and $\overline{\tau}$ is a vector containing the average time to exit each of the transient states. It is also important to determine where exits from the basal facets occur. This information is contained in

$$\overline{\pi}^A = \overline{p}_0^T \cdot (\mathbf{T} - \mathbf{I})^{-1} \cdot \mathbf{R} \quad , \tag{2}$$

where $\overline{\pi}^A$ contains the probability that each absorbing state will be occupied at the end of the process.

To construct **T** and **R**, we used $r_{ij} = v_0 \exp(-E_{B,ij}/kT)$ to calculate the transition rate between each pair of transient states or transient and absorbing states *i* and *j*. We calculated the rates at the experimental temperature of 363 K.[37] The values of $E_{B,ij}$ are taken from the DFT calculations summarized in **Table 1** and **Figures 5** and **6**.

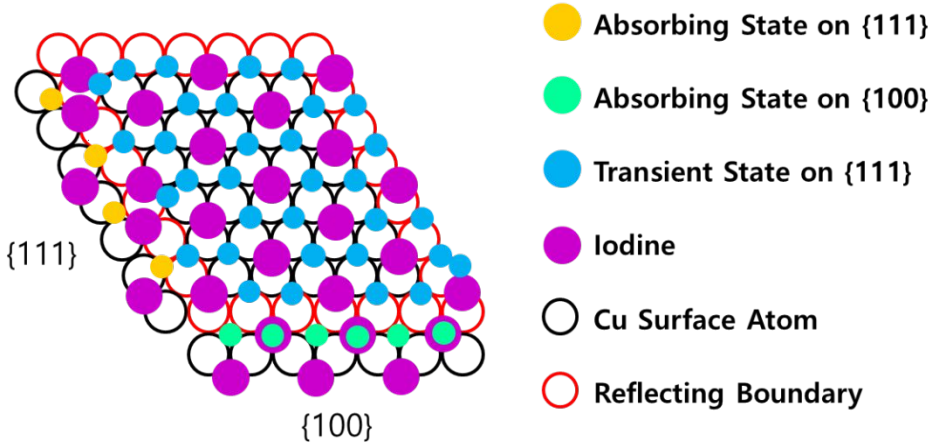

The basal plane of a plate,

Figure 7. Lay-out for a unit cell in MFPT calculations.

Figure 7 shows an example lay-out for a small unit cell in our MFPT calculations and indicates the transient states on the basal {111} facet, as well as the absorbing states on the {111} and {100} facets. We consider the situation in which iodine atoms are placed on fcc sites on the basal plane and the {111} side facet. Our unit cell represents one third of a hexagonal basal facet, as can be seen more clearly in **Figure S10**, and we apply reflecting boundary conditions for diffusion to transient states on sites that would cross a boundary indicated in **Figure 7**. **Table 2** shows average transit rates (t_M^{-1}) as a function of the plate dimension. **Figure S11** shows the rate t_M^{-1} as a function of the number of transient states (plate dimension). Since we consider every possible Cu binding site on (one-third of) the basal plane of a Cu plate, calculations for plate sizes beyond 200 nm become computationally expensive. We extrapolated our results to obtain MFPTs for large plates. **Figure S11** shows that the extrapolation model fits well to our calculated rates.

Table 2. Calculated inter-facet diffusion rates from basal {111} to side {111} and {100} facets in a hexagonal plate.

Plate Width (nm)	Inter-Facet Diffusion Rate (1/s)
40	1.07×10^6
200	3.72×10^5
500	8.54×10^4
1000	2.26×10^4
1500	1.02×10^4
4800	1.00×10^3

To assess the lateral dimensions of the plates, we need to compare the MFPT to the Cu deposition rate in the syntheses. In similar experiments to those for plate synthesis,[37,47,48] the initial deposition rate in a synthesis solution of Cu nanowires including Cl^- and HDA was estimated to be around $10^4 - 10^5/s$ and we expect the addition of I^- to the solution for growing Cu plates to decrease the reduction (deposition) rate.[37] Thus, we approximate the initial deposition rate to be 10^4/s in the synthesis of Cu plates. This rate decreases over time as Cu salt is depleted to grow the plates, so we expect a reasonable range of deposition rates to be $10^3 - 10^4$ s^{-1}. Using our model, the inter-facet diffusion rate becomes equal to a deposition rate of 10^4 s^{-1} when the plate dimension is 1.5 μm and the plates can achieve a lateral dimension of 4.8 μm when the deposition rate is 10^3 s^{-1}. Plates with dimensions in the 1-10 micron range were observed experimentally,[37] in agreement with our results.

In addition to calculating the MFPT and inter-facet transit rates, we assessed the probability for a Cu atom on a basal {111} late facet to access either a {100} or {111} facet using Equation (2). These calculations indicate that for a hexagonal plate, the probability of a Cu atom to go from the basal plane to a {111} side is 0.05 and the probability of the atom to go to a {100} side is 0.95. In addition to their strong binding preference, this diffusion preference also contributes to the preferred accumulation of Cu atoms on the {100} side facets. However, even with such a strong binding and transport preference to Cu(100), we still expect the plates will undergo a series of different shapes as they grow laterally, as we see in **Figure 4.**

Conclusion

In summary, we quantified several aspects that facilitate the I-mediated growth of Cu microplates. First, we showed that a Cu adatom binds more strongly to hcp hollow sites than fcc hollow sites on iodine-covered Cu(111). This feature promotes the formation of stacking faults during seed and plate growth which, in turn, promotes 2D growth. We also found that iodine adsorption leads to strong Cu atom binding and prohibitively slow diffusion of Cu atoms on Cu(100). Incorporating these insights into analog experiments, in which we initiated the growth of Cu plates from small seeds consisting of magnetic spheres, we found that two or more stacking faults are required for lateral plate growth. Moreover, plates can take on a variety of shapes during growth: from triangular and truncated triangular to round and hexagonal. Though the diffusion of Cu atoms is slower on I-covered Cu(111) than on the bare surface,[46] it is still relatively rapid and, as we showed in our absorbing Markov chain calculations, it is rapid enough to promote lateral growth of microplates with dimensions in the 1-5 micron range. Therefore, we conclude the adsorption of iodine on Cu surfaces favors the anisotropic growth of thin Cu plates by influencing on both seed formation and growth stages.

Computational methods

All DFT calculations were carried out using the Vienna Ab initio Simulation Package (VASP) with the projector augmented-wave (PAW) method.[49–53] The generalized gradient approximation (GGA) by Perdew, Burke, and Ernzerhof (PBE) was used for the exchange-correlation functional.[54] 400 eV was used as an optimal value for the energy cut-off for the plane-wave basis set. We also used Monkhorst-Pack grids for integration over the first Brillouin zone.[55] A (12 x 12 x 12) k-point mesh was used for calculations for bulk Cu. A cubic unit cell with a side length of 20 Å and a single *k* point was used to calculate the energy of an isolated Cu atom and a single I_2 molecule in the gas phase.

We used a periodic Cu slab with six Cu layers to describe the flat Cu surfaces. The bottom three layers of the slab were fixed to describe the bulk positions and the top three layers and adsorbed species were allowed to fully relax during structural optimization. Structural optimization was performed within a value of 10^{-6} eV for the energy convergence criterion and 0.01 eV/Å was used for the force convergence criterion. The Cu lattice constant was calculated to be 3.64 Å, which is well matched with other theoretical values using the GGA functional[56–58] and has less than 0.6 % difference from the observed experimental values of 3.615 Å.[59] A (4 x 6) surface unit cell size was used for both Cu(100) and Cu(111). The optimal *k*-point mesh was determined to be (6 x 4 x 1) for Cu(100) and (7 x 5 x 1) for Cu(111). A vacuum space of 15 Å was included to separate periodic slabs and a dipole correction along the surface normal was also employed to avoid interactions between periodic slabs.

To calculate the binding energy for I and Cu atoms on the Cu surfaces, we used,

$$E_{bind,X} = \frac{1}{N_X}[E_{slab+X} - (E_{slab} + N_X E_X)] \quad , \tag{13}$$

where X can be either Cu or I absorbed on the Cu surface, E_X is the energy of an isolated X in vacuum (here, $E_X = \frac{1}{2}E_{X_2}$ for X = I), N_X is the number of X on the Cu surface, E_{slab} is the energy of the Cu slab – either a bare or I-covered Cu slab, and E_{slab+X} is the energy of an optimized Cu slab with X. Table S5 in the ESI lists the convergence test for the binding of a Cu adatom on Cu surfaces, with regarding to the energy cut-off, *k*-point mesh, and vacuum spacing.

To include long-range van der Waals (vdW) interactions in our DFT calculations, we used the DFT-D2 method of Grimme.[60] Especially for the screening effect of Cu, we employed the dispersion coefficient and the vdW radius suggested by Ruiz et al.,[61] while the default values of these parameters are those suggested by Grimme for? the other elements. The cutoff radius for the vdW interactions was 40.0 Å.

To identify a transition state and energy barrier for the surface diffusion of a Cu adatom on the Cu surfaces, we employed the climbing nudged elastic band (CI-NEB) method with using 3 – 6 images for an individual diffusion pathway.[38] Vibrational frequencies were calculated to confirm a single imaginary frequency for each identified transition state. The spring constant was set to 5.0 eV/Å^2 and all CI-NEB calculations are converged when the force on each atom was less than 0.05 eV/Å.

To quantify diffusion between facets on plate-like Cu crystals, we created two Cu inter-facet slabs. One has {111} on the top and {111} and {100} on each side – **Figure S5(a)**, while the other has {100} on the top and {111} on both sides – **Figure S5(b)**. The former was used for calculations of the {111}-{111} edge, and the later was used for the {111}-{100} edge. The inter-facet slabs consisted of six Cu layers. To optimize the slab configurations, we allowed the

outer two Cu layers and all absorbed I atoms to fully relax, while fixing the bottom two Cu layers, their associated I atoms, and Cu atoms in the middle of the slab. Slabs were continuous in one dimension only – parallel to the inter-facet edges. We included a vacuum spacing in the z direction normal to the top facet and in the direction perpendicular to the inter-facet edge. We used a (4 x 1 x 1) and (1 x 4 x 1) *k*-point mesh for the slabs in **Figure S5(a)** and **Figure S5(b)**, respectively. Convergence tests with respect to *k*-points and vacuum space for the inter-facet slabs are summarized in **Tables S5 and S6**.

Acknowledgements

This work is funded by the Department of Energy, Office of Basic Energy Sciences, Materials Science Division, Grant DE FG02-07ER46414 (J.K.). J.K. acknowledges training provided by the Computational Materials Education and Training (CoMET) NSF Research Traineeship (DGE-1449785). This work used the Extreme Science and Engineering Discovery Environment (XSEDE), which is supported by National Science Foundation grant number ACI-1548562.

References

1 I. Pastoriza-Santos and L. M. Liz-Marzan, *J. Mater. Chem.*, 2008, **18**, 1724–1737.

2 Y. Chen, Z. Fan, Z. Zhang, W. Niu, C. Li, N. Yang, B. Chen and H. Zhang, *Chem. Rev.*, 2018, **118**, 6409–6455.

3 R. D. Neal, R. A. Hughes, A. S. Preston, S. D. Golze, T. B. Demille and S. Neretina, *J. Mater. Chem. C*, 2021, **9**, 12974–13012.

4 T. Wang, M. Park, Q. Yu, J. Zhang and Y. Yang, *Mater. Today Adv.*, 2020, **8**, 100092.

5 Q. Yu and Y. Yang, *ChemNanoMat*, 2020, **6**, 1683–1711.

6 H. Tian, Y. Yu, Q. Wang, J. Li, P. Rao, R. Li, Y. Du, C. Jia, J. Luo, P. Deng, Y. Shen and X. Tian, *Int. J. Hydrogen Energy*, 2021, 46, 31202–31215.

7 F. Lv, B. Huang, J. Feng, W. Zhang, K. Wang, N. Li, J. Zhou, P. Zhou, W. Yang, Y. Du, D. Su and S. Guo, *Natl. Sci. Rev.*, , DOI:10.1093/nsr/nwab019.

8 F. Qin, Z. Yan, J. Fan, J. Cai and X. Zhu, *Macromol. Mater. Eng.*, 2021, **306**, 2000607.

9 X. Huang, S. Tang, X. Mu, Y. Dai, G. Chen, Z. Zhou, F. Ruan, Z. Yang and N. Zheng, *Nat. Nanotechnol.*, 2011, **6**, 28–32.

10 Y. Shi, Z. Lyu, M. Zhao, R. Chen, Q. N. Nguyen and Y. Xia, *Noble-Metal Nanocrystals with Controlled Shapes for Catalytic and Electrocatalytic Applications*, 2021, vol. 121.

11 J. Yin, J. Wang, Y. Ma, J. Yu, J. Zhou and Z. Fan, *ACS Mater. Lett.*, 2021, **3**, 121–133.

12 P. K. Kalambate, J. Noiphung, N. Rodthongkum, N. Larpant, P. Thirabowonkitphithan, T. Rojanarata, M. Hasan, Y. Huang and W. Laiwattanapaisal, *TrAC - Trends Anal. Chem.*, 2021, **143**, 116403.

13 Y. Zhang, H. Lu, F. Yang, Y. Cheng, W. Dai, X. Meng, H. Dong and X. Zhang, *Anal. Chim. Acta*, 2020, **1139**, 164–168.

14 T. A. Mai Ngoc, D. T. D. Nguyen, V. K. T. Ngo, P. P. Nguyen Thi, D. H. Nguyen and M. T. Nguyen-Le, *Plasmonics*, 2020, **15**, 2185–2194.

15 C. Gao, Z. Lu, Y. Liu, Q. Zhang, M. Chi, Q. Cheng and Y. Yin, *Angew. Chemie - Int. Ed.*, 2012, **51**, 5629–5633.

16 C. L. Lee, K. C. Chang and C. M. Syu, *Colloids Surfaces A Physicochem. Eng. Asp.*, 2011, **381**, 85–91.

17 M. Chen, S. Tang, Z. Guo, X. Wang, S. Mo, X. Huang, G. Liu and N. Zheng, *Adv. Mater.*, 2014, **26**, 8210–8216.

18 B. Pelaz, V. Grazu, A. Ibarra, C. Magen, P. Del Pino and J. M. De La Fuente, *Langmuir*, 2012, **28**, 8965–8970.

19 I. S. Raja, M. S. Kang, K. S. Kim and Y. J. Jung, *Cancers (Basel).*, 2020, **12**, 1657.

20 L. Cheng, X. Wang, F. Gong, T. Liu and Z. Liu, *Adv. Mater.*, 2020, **32**, 1–23.

21 Z. Zhang, J. Du, J. Li, X. Huang, T. Kang, C. Zhang, S. Wang, O. O. Ajao, W. J. Wang and P. Liu, *Prog. Polym. Sci.*, 2021, 114, 101360.

22 Q. Zhang, L. Long, G. Zhang, Z. Y. Li and Y. Zheng, *CrystEngComm*, 2019, **22**, 173–177.

23 Q. Zhang, Y. Hu, S. Guo, J. Goebl and Y. Yin, *Nano Lett.*, 2010, **10**, 5037–5042.

24 F. Qin, T. Zhao, R. Jiang, N. Jiang, Q. Ruan, J. Wang, L. D. Sun, C. H. Yan and H. Q. Lin, *Adv. Opt. Mater.*, 2016, **4**, 76–85.

25 T. Yu, Z. Wu and W. S. Kim, *RSC Adv.*, 2014, **4**, 37516–37521.

26 J. Wang, X. Guo, Y. He, M. Jiang and R. Sun, *RSC Adv.*, 2017, **7**, 40249–40254.

27 G. S. Métraux and C. A. Mirkin, *Adv. Mater.*, 2005, **17**, 412–415.

28 S. Xu, X. Sun, H. Ye, T. You, X. Song and S. Sun, *Mater. Chem. Phys.*, 2010, **120**, 1–5.

29 Y. Xiong, I. Washio, J. Chen, M. Sadilek and Y. Xia, *Angew. Chem. Int. Ed. Engl.*, 2007, **46**, 4917–21.

30 Y. Xiong, J. M. McLellan, J. Chen, Y. Yin, Z. Y. Li and Y. Xia, *J. Am. Chem. Soc.*, 2005, **127**, 17118–17127.

31 B. Y. Xiong and Y. Xia, *Adv. Mater.*, 2007, **19**, 3385–3391.

32 C. Lofton and W. Sigmund, *Adv. Funct. Mater.*, 2005, **15**, 1197–1208.

33 T. C. R. Rocha and D. Zanchet, *J. Phys. Chem. C*, 2007, **111**, 6989–6993.

34 S. D. Golze, R. A. Hughes, S. Rouvimov, R. D. Neal, T. B. Demille and S. Neretina, *Nano Lett.*, 2019, **19**, 5653–5660.

35 T. Tan, S. Zhang, J. Wang, Y. Zheng, H. Lai, J. Liu, F. Qin and C. Wang, *Nanoscale*, 2021, **13**, 195–205.

36 D. Aherne, D. M. Ledwith, M. Gara and J. M. Kelly, *Adv. Funct. Mater.*, 2008, **18**, 2005–2016.

37 M. J. Kim, M. A. Cruz, Z. Chen, H. Xu, M. Brown, K. A. Fichthorn and B. J. Wiley, *Chem. Mater.*, 2021, **33**, 881–891.

38 G. Henkelman, B. P. Uberuaga, H. Jonsson, H. Jónsson, H. Jo and H. Jonsson, *J. Chem. Phys.*, 2000, **113**, 9901–9904.

39 J. Goebl, Q. Zhang, L. He and Y. Yin, *Angew. Chemie*, 2012, **124**, 567–570.

40 A. A. I. Kirkland, D. A. Jefferson, D. G. Duff, P. P. Edwards, I. Gameson, G. Johnson, D. J. Smith, S. P. Mathematical and P. Sciences, *Proc. R. Soc. London. Ser. A Math. Phys. Sci.*, 1993, **440**, 589–609.

41 J. Zeng, J. Tao, W. Li, J. Grant, P. Wang, Y. Zhu and Y. Xia, *Chem. - An Asian J.*, 2011, **6**, 376–379.

42 J. G. Kemeny and J. L. Snell, *Finite Markov Chains.*, Springer-Verlag, New York, 1976.

43 M. A. Novotny, *Phys. Rev. Lett.*, 1995, **74**, 1–5.

44 K. A. Fichthorn and Y. Lin, *J. Chem. Phys.*, 2013, **138**, 164104.

45 X. Qi, Z. Chen, T. Yan and K. A. Fichthorn, *ACS Nano*, 2019, **13**, 4647–4656.

46 J. Kim, J. Cui and K. A. Fichthorn, *ACS Nano*, , DOI:10.1021/acsnano.1c07425.

47 M. J. Kim, S. Alvarez, T. Yan, V. Tadepalli, K. A. Fichthorn and B. J. Wiley, *Chem. Mater.*, 2018, **30**, 2809–2818.

48 M. J. Kim, S. Alvarez, Z. Chen, K. A. Fichthorn and B. J. Wiley, *J. Am. Chem. Soc.*, 2018, **140**, 14740–14746.

49 G. Kresse and J. Hafner, *Phys. Rev. B*, 1993, **47**, 558–561.

50 G. Kresse and J. Hafner, *Phys. Rev. B*, 1994, **49**, 14251–14269.

51 G. Kresse and J. Furthmüller, *Phys. Rev. B*, 1996, **54**, 11169–11186.

52 P. E. Blöchl, *Phys. Rev. B*, 1994, **50**, 17953.

53 G. Kresse and D. Joubert, *Phys. Rev. B*, 1999, **59**, 1758–1775.

54 J. P. Perdew, K. Burke and M. Ernzerhof, *Phys. Rev. Lett.*, 1996, **77**, 3865–3868.

55 H. J. Monkhorst and J. D. Pack, *Phys. Rev. B*, 1976, **13**, 5188.

56 Z. Xiong, S. Shi, C. Ouyang, M. Lei, L. Hu, Y. Ji, Z. Wang and L. Chen, *Phys. Lett. A*, 2005, **337**, 247–255.

57 J. L. F. Da Silva, C. Stampfl and M. Scheffler, *Surf. Sci.*, 2006, **600**, 703–715.

58 H. Y. Xiao, X. T. Zu, X. He and F. Gao, *Chem. Phys.*, 2006, **325**, 519.

59 K. Hermann, *Crystallography and Surface Structure: An Introduction for Surface Scientists and Nanoscientists*, Wiley-VCH, Weinheim, Germany, 2011.

60 S. Grimme, *J. Comput. Chem.*, 2006, **27**, 1787–1799.

61 V. G. Ruiz, W. Liu, E. Zojer, M. Scheffler and A. Tkatchenko, *Phys. Rev. Lett.*, 2012, **108**, 146103.